

# Chemical evolution of the Galactic bulge with different stellar populations

M. Molero<sup>1,2,3</sup>, F. Matteucci<sup>2,3</sup>, E. Spitoni<sup>3</sup>, A. Rojas-Arriagada<sup>4,5,6,7</sup>, and R. M. Rich<sup>8</sup>

<sup>1</sup> Institut für Kernphysik, Technische Universität Darmstadt, Schlossgartenstr. 2, Darmstadt 64289, Germany  
e-mail: mmolero@theorie.ikp.physik.tu-darmstadt.de

<sup>2</sup> Dipartimento di Fisica, Sezione di Astronomia, Università degli Studi di Trieste, Via G. B. Tiepolo 11, 34143 Trieste, Italy

<sup>3</sup> INAF, Osservatorio Astronomico di Trieste, Via Tiepolo 11, 34131 Trieste, Italy

<sup>4</sup> Departamento de Física, Universidad de Santiago de Chile, Av. Victor Jara 3659, Santiago, Chile

<sup>5</sup> Millennium Institute of Astrophysics, Av. Vicuña Mackenna 4860, 82-0436 Macul, Santiago, Chile

<sup>6</sup> Center for Interdisciplinary Research in Astrophysics and Space Exploration (CIRAS), Universidad de Santiago de Chile, Santiago, Chile

<sup>7</sup> Núcleo Milenio ERIS, Santiago, Chile

<sup>8</sup> Department of Physics and Astronomy, UCLA, 430 Portola Plaza, Box 951547, Los Angeles, CA 90095-1547, USA

Received 17 April 2024 / Accepted 13 May 2024

## ABSTRACT

**Context.** The metallicity distribution function (MDF) of the Galactic bulge is characterized by a multi-peak shape, with a metal-poor peak centered at  $[Fe/H] \sim -0.3$  dex and a metal-rich peak centered at  $[Fe/H] \sim +0.3$  dex. The bimodality of the MDF is also reflected in the  $[\alpha/Fe]$  versus  $[Fe/H]$  abundance ratios, suggesting the presence of different stellar populations in the bulge.

**Aims.** In this work we aim to reproduce the observed MDF of the Galactic bulge by testing a scenario in which the metal-poor component of the bulge is formed by stars formed in situ, during a strong burst of star formation, while the metal-rich population is formed by stars created in situ during a second burst of star formation and/or stars accreted from the innermost part of the Galactic disk as an effect of a growing bar.

**Methods.** We adopted a chemical evolution model that is able to follow the evolution of several chemical species with detailed nucleosynthesis prescriptions. In particular, because of the importance of the production of Fe in constraining the MDF, close attention is paid to the production of this element in both Type Ia supernovae and massive stars. In particular, we included yields from rotating massive stars with different rotational velocity prescriptions. Our model also takes the infall and outflow of gas into account, as well as the effect of stellar migration. Results are compared to  $\sim 13\,000$  stars from the SDSS/APOGEE survey that belong to the region located at a Galactocentric distance  $R_{GC} \leq 3.5$  kpc.

**Results.** We successfully reproduce the observed double-peak shape of the bulge MDF as well as the abundance trends of the  $\alpha$  elements relative to Fe by assuming both (i) a multi-burst star formation history with a quenching of the first burst of  $\sim 10^2$  Myr and (ii) migration of stars from the innermost part of the Milky Way disk, as an effect of a growing bar. According to our results, the fraction of the stellar mass of the bulge-bar that belongs to the inner disk is  $\sim 40\%$ . In terms of the nucleosynthesis, we conclude that models that assume either no rotation for massive stars or a distribution of rotational velocities that favors slow rotation at high metallicities best reproduce the observed MDF as well as the  $[\alpha/Fe]$  and the  $[Ce/Fe]$  versus  $[Fe/H]$  abundance patterns.

**Key words.** stars: chemically peculiar – ISM: abundances – evolution – Galaxy: bulge – Galaxy: evolution – Galaxy: formation

## 1. Introduction

The formation and evolution of the Milky Way (MW) bulge has been the subject of intense studies over the last decade. According to the original picture, the Galactic bulge can be considered a classical bulge, namely a spheroidal remnant of mergers of primordial structures in a  $\Lambda$  cold dark matter context ( $\Lambda$ CDM; [Ortolani et al. 1995](#); [Baugh et al. 1996](#); [Abadi et al. 2003a,b](#)). However, both observations of our own bulge (e.g., [Binney et al. 1991](#); [Bissantz & Gerhard 2002](#); [López-Corredoira et al. 2005](#)) and at higher redshifts (e.g., [Tacchella et al. 2015](#); [Nelson et al. 2016](#); [Shen et al. 2024](#)) point toward a much more complex picture. Contrary to classical bulges, pseudo-bulges should form from disk stars due to the vertical instability of a stellar bar ([Combes et al. 1990](#)). This scenario should lead to the formation of a triaxial boxy bar structure, the so-called boxy/peanut (B/P) shape of the

Galactic bulge (e.g., [Weiland et al. 1994](#); [McWilliam & Zoccali 2010](#); [Wegg & Gerhard 2013](#); [Ness & Lang 2016](#)), which in  $N$ -body simulations has also been seen to form from barred stellar disk galaxies ([Raha et al. 1991](#); [O'Neill & Dubinski 2003](#); [Athanassoula 2005](#); [Shen et al. 2010](#); [Ciambur et al. 2021](#); [Ghosh et al. 2023](#)). Moreover, fully formed bulges or a high central star formation (SF) are observed in galaxies at redshift  $z \sim 2$  ([Tadaki et al. 2017](#)); this suggests that those bulges assembled before the formation of the bar, which, in the case of MW-type galaxies, happened at  $z \sim 1$  (i.e.,  $\sim 8$  Gyr ago). Therefore, the mechanism responsible for the creation of such structures should be a fast and strong primordial collapse of gas responsible for at least one rapid SF episode.

The Galactic bulge region can be very hard to observe because of heavy extinction and crowding. Nevertheless, several spectroscopic (e.g., BRAVA, [Rich et al. 2008](#); [Kunder et al. 2012](#), Gaia-ESO, [Gilmore et al. 2012](#), APOGEE,

Majewski et al. 2017, ARGOS, Freeman et al. 2013, GIBS, Zoccali et al. 2014) and photometric (e.g., the VVVX survey; Minniti et al. 2010) surveys have been developed to shed light on the history of the bulge (see Barbuy et al. 2018 for a review of the different surveys). The picture that emerges from observations appears, however, to be complex. The metallicity distribution function (MDF) of stars observed in the bulge region has a bimodal shape (observed for the first time by Hill et al. 2011 and later confirmed in a large number of studies, e.g., Bensby et al. 2011; Uttenthaler et al. 2012; Gonzalez et al. 2015; Rojas-Arriagada et al. 2017, 2019, 2020; Zoccali et al. 2017; Queiroz et al. 2020, 2021; Johnson et al. 2020, 2022), which can be an indication of two (or more) stellar populations: a metal-rich (MR) population centered at  $[Fe/H] \sim 0.25$  dex and a metal-poor (MP) population centered at  $[Fe/H] \sim -0.3$  dex. The two stellar populations can also have different kinematics, with the MR one rapidly rotating and dynamically cold and the MP one dynamically hotter and rotating more slowly. Babusiaux et al. (2010), who inspected the kinematics of the large sample of over 500 red-giant branch (RGB) stars presented in Zoccali et al. (2008), concluded that the MR population shows a vertex deviation compatible with the MW bar (it is worth noting that vertex deviation was first seen by Zhao et al. 1996; Soto et al. 2007), while the MP population is compatible with a spheroid (and/or a thick disk). Moreover, results of the chemodynamical model presented by Portail et al. (2017) show that MR stars (with  $[Fe/H] \geq -0.5$  dex) are strongly barred with dynamical properties consistent with a common disk origin, while MP stars (with  $[Fe/H] < -0.5$  dex) show more kinematic variations with metallicity, which is interpreted as being due to the contributions from different stellar populations.

As pointed out by Baba & Kawata (2020), if the Galactic bar significantly impacts the dynamic of the stars in the bulge (and therefore also in the inner disk; e.g., Minchev et al. 2016), identifying its formation epoch should provide important insights into the history of the MW. As discussed above, the time of the formation of the Galactic bar is highly uncertain. From the distribution of infrared carbon stars, Cole & Weinberg (2002) estimated an age of  $\sim 2$  Gyr. From observations of luminous face-on spiral galaxies, Sheth et al. (2008) analyzed the variation with redshift of the fraction of galactic bars and estimated that the bar in spirals with masses similar to that of the MW should form at  $z \approx 1$  ( $\sim 8$  Gyr ago; a result that was confirmed by the zoom-in cosmological simulations in Kraljic et al. 2012). More recently, the bar formation and building epoch were also estimated to have happened 8–9 Gyr ago from a study of the *Gaia* Data Release (DR) 2 set of long-period variables by Grady et al. (2020), though the long-period variables in the bar are generally more MR and hence may be older at a given luminosity. It should be pointed out that the age of the stars in the bar does not necessarily correspond to the age of the bar itself, since the bar can capture stars that formed before its formation (though the absence of SF in the bar cannot be excluded a priori; see e.g., Anderson et al. 2020). This process is described by Chiba et al. (2021, see also Chiba & Schönrich 2021, 2022). According to the authors, the bar experiences angular momentum loss due to dynamical friction from the dark matter halo, which slows its pattern speed,  $\Omega_p$  (see also Hernquist & Weinberg 1992; Debattista & Sellwood 2000; Martinez-Valpuesta et al. 2006). When the bar slows down, the resonance sweeps radially outward in radius throughout the disk, sequentially capturing and dragging new stars. A fraction of stars that are trapped in the corotation radius can then be captured by the bar itself. So, from a chemical point of view, stars in the bar should reflect the com-

position of the location where they were trapped (assuming it is also where they were born). As a consequence, if the bar captures stars from the disk, those stars may have the same composition and age as the disk.

The first chemical evolution model for the Galactic bulge that released the instantaneous recycling approximation was developed by Matteucci & Brocato (1990) to explain the results of Rich (1988, 1990). Matteucci & Brocato (1990) suggested that the bulge formed during a strong burst of SF on a short timescale ( $\sim 0.5$  Gyr), with a more top-heavy initial mass function (IMF) than that of the solar neighborhood (e.g., Scalo 1986). Their model predicted a plateau in the  $[\alpha/Fe]$  ratios in bulge stars longer than that in the solar vicinity, which was later confirmed by McWilliam & Rich (1994) and is now an observationally established fact. The prescriptions of the model were then confirmed in updated versions (e.g., Ballero et al. 2007; Cescutti & Matteucci 2011). Later on, more chemical evolution models started to try modeling the bimodal MDF of the bulge (e.g., Grieco et al. 2012a, 2015; Tsujimoto & Bekki 2012) in an attempt to explain it as due to a second infall and/or accretion episode. More recently, Matteucci et al. (2019) successfully reproduced the MR peak of the bulge MDF by assuming a pause of  $\sim 250$  Myr in the SF of the bulge and proposed a scenario in which the MR population is made of either stars formed in a second burst after the pause or stars formed in the inner disk and transported into the bulge during the early secular evolution of the bar.

The main goal of this work is to confirm (or disprove) this hypothesis by adopting a chemical evolution model that includes both multiple SF episodes and the accretion of stars from the MW disk. The bulge has a complex structure with a vertical abundance gradient (e.g., Zoccali et al. 2008, 2017; Ness et al. 2013; Johnson et al. 2014, 2020, 2022). Our models do not address this vertical gradient, but they may shed light on some of the physical processes that could cause a vertical abundance gradient.

The paper is organized as follows: In Sect. 2 we describe the chemical evolution models and their prescriptions. In Sect. 3 we present the results regarding the hypothesis that bulge stars formed only in situ, while in Sect. 4 we present the results for accreted stars. Finally, in Sect. 5 we draw some conclusions.

## 2. Observational data

We compared our model predictions to the APOGEE DR16 sample of bulge stars of Rojas-Arriagada et al. (2020). We refer the reader to that paper for the full details concerning the description of APOGEE survey data and the sample selection. We provide a brief summary here. APOGEE is an SDSS-III and SDSS-IV high-resolution near-infrared spectroscopic survey of resolved stellar populations in the MW and some of its satellites. The main targets of the survey are giant stars, RGB, red clump, and asymptotic giant branch (AGB) stars, which allow large spatial regions to be mapped. The targets were observed in the  $H$ -band using two twin high resolution ( $R \sim 22\,500$ ) spectrographs operating at the Apache Point Observatory's 2.5 m Sloan Telescope and Las Campanas Observatory's 2.5 Irénée du Pont telescope. APOGEE spectra are extracted, wavelength calibrated and RV corrected using a custom pipeline (Nidever et al. 2015). Stellar atmospheric parameters and abundances of up to 26 elements are measured using the APOGEE Stellar Parameters and Chemical Abundances Pipeline (ASPCAP; García Pérez et al. 2016).

In Rojas-Arriagada et al. (2020) an initial sample was selected within the region  $|l| < 16^\circ$  and  $|b| < 15^\circ$ . The individual

fields are not homogeneously distributed over that region but are concentrated toward the midplane, where extinction levels are high and the near-infrared capabilities of APOGEE can sample bulge stellar populations through the dust veil. A set of spectrophotometric distances were computed using an isochrone fitting technique. In order to secure reliable ASPCAP parameters, several cuts based on rather technical flags were implemented. An additional cut on surface gravity, removing stars with  $\log(g) > 2.2$  dex, was adopted to ensure a sample free of selection and analysis bias. Finally, from the analysis of several kinematic and orbital parameters, a cut on Galactocentric distance of  $R_{\text{GC}} < 3.5 \text{ kpc}$  was adopted to select a sample of stars spatially located in the bulge region. The bulge sample so defined consists on 13 031 stars.

We emphasize that while only metallicity was used to study the shape of the bulge MDF in Rojas-Arriagada et al. (2020), the complete assortment of abundances is available for the selected sample. On the other hand, although there is a new public APOGEE data release (DR17) available, we adopted the values from DR16 to for the sake homogeneity and consistence with the definition of the sample, which is based on the parameters from the DR16. In the following, we compare our model predictions with both the MDF and the abundances ratios of the  $\alpha$  elements Mg, O, Al, and Si as well as with the neutron capture element Ce. We note that this model does not attempt to consider any spatial variation in the Rojas-Arriagada et al. (2020) abundance distribution.

### 3. The model

The chemical evolution model adopted for the Galactic bulge is similar to the one developed by Grieco et al. (2012b) and later updated by Matteucci et al. (2019) see also Ballero et al. 2007; Cescutti & Matteucci 2011). We assumed that the bulge forms by fast infall of gas with a timescale  $\tau_b = 0.1 \text{ Gyr}$ . The gas is very efficiently converted into stars with a SF parametrized by a Schmidt-Kennicutt law (Schmidt 1959; Kennicutt 1998) with exponent  $k = 1.4$  and with an efficiency of SF  $v = 25 \text{ Gyr}^{-1}$ , much higher than what assumed in the thin disk. The adopted IMF is a Chabrier (2003), though we investigated the possibility of using a Salpeter (1955) IMF, as done in the previous chemical evolution works.

After the first main SF episode, mainly responsible for the formation of the MP population observed in the MDF, a second SF burst is present with a delay with respect to the first of order  $10^2 \text{ Myr}$ . The second burst is partially responsible for the creation of the MR population but, as we show in the next sections, it is not enough to completely populate the MR peak in the MDF. Here, we assumed that a fraction of stars originally belonging to the innermost part of the MW disk also populates the Galactic bulge and is partially responsible for the formation of the MR peak. The disk is modeled as described in Molero et al. (2023), by means of the revised two-infall model of Palla et al. (2020 see also Spitoni et al. 2019, 2021). The model assumes that the MW disk forms as a result of two distinct accretion episodes of gas. The first one, with a timescale of  $\tau_{\text{d},1} = 1 \text{ Gyr}$ , is responsible for the formation of the chemically thick disk (namely the high- $\alpha$  sequence observed in the  $[\alpha/\text{Fe}]$  versus  $[\text{Fe}/\text{H}]$  plane), while the second infall episode, delayed with respect to the first one by  $\sim 3.25 \text{ Gyr}$ , is responsible for the formation of the chemically thin disk (the low- $\alpha$  sequence). The timescale for the second infall episode is a function of the Galactocentric distance

(see Chiappini et al. 2001):

$$\tau_{\text{d},2}(R) = \left( 1.033 \frac{R}{\text{kpc}} - 1.267 \right) \text{ Gyr}, \quad (1)$$

so it is shorter toward inner regions.

For both the Galactic bulge and the inner disk the same nucleosynthesis prescriptions are adopted, similar to those adopted by Molero et al. (2023). We refer to that paper for a more detailed discussion.

In summary, we used:

- The non-rotational set of yields of the FRUITY database (Cristallo et al. 2009, 2011, 2015) for low- and intermediate-mass stars (LIMSS;  $M \leq 8 M_{\odot}$ ).
- The Limongi & Chieffi (2018) recommended yield set  $R$  with mass-loss and rotation for massive stars ( $M \geq 13 M_{\odot}$ ). Here, we also assumed that 20% of massive stars with  $10-25 M_{\odot}$  explode as magneto-rotational supernovae (SNe), with yields from the Nishimura et al. (2017) model L0.75.
- Yields from the Iwamoto et al. (1999) model W7 for Type Ia SNe.
- For merging neutron stars (MNSs), we adopted yields scaled to those of Sr from the kilonova AT2017gfo measured by Watson et al. (2019, see Molero et al. 2021). MNSs are assumed to merge with a delay time distribution function (see Simonetti et al. 2019).

In particular, for massive stars, besides testing the three sets of yields of Limongi & Chieffi (2018) corresponding to three initial rotational velocities (0, 150, and  $300 \text{ km s}^{-1}$ ), three more sets have been considered, corresponding to three different theoretical distributions for the initial rotational velocities. These new sets of yields were obtained by assuming that the probability that a star rotates at a certain speed is a function of the metallicity,  $Z$ , with faster initial rotational velocities being most likely at lower  $Z$ . In this way, we obtained the first two distributions (DIS 1 and DIS 2) reported in Fig. 1. In DIS 2, velocities of  $0 \text{ km s}^{-1}$  and of  $150 \text{ km s}^{-1}$  are slightly more likely than in DIS 1 at intermediate and high metallicities. The third distribution shown in the figure, DIS 3, is the one adopted by Romano et al. (2019) for studying the CNO isotopes, according to which rotation becomes negligible beyond a metallicity threshold equal to  $Z = 3.236 \times 10^{-3}$  (corresponding to  $[\text{Fe}/\text{H}] = -1 \text{ dex}$ ). All the three distributions are supported by the fact that massive stars are expected to rotate faster at lower metallicities, where they are more compact (see Klencki et al. 2020). This view is supported both theoretically (Frischknecht et al. 2016) and by the observations of an increase ratio of Be/B-type star with increasing metallicity (Martayan et al. 2007a,b), as well as by the presence of faster rotating massive stars in the Small Magellanic Cloud than in the MW (Hunter et al. 2008) and by observations of stars in the globular cluster NGC6522 with high abundances of  $s$ -process elements (Chiappini et al. 2011). We assumed a flat distribution of the initial rotational velocities with the stellar mass. Although this is a simplification, it still finds agreement in theoretical computations (e.g., Frischknecht et al. 2016), which show that, for the same metallicity and initial ratio of surface velocity to critical velocity ( $v_{\text{ini}}/v_{\text{crit}}$ ), the changes in the surface velocity during the MS phase as a function of mass are relatively small and in any case less than the variations as a function of metallicity.

As mentioned in Sect. 1, the MW bar does not exhibit static rotation. Indeed, simulations of the Galactic bar in the presence of dark matter indicate that the bar experiences angular momentum loss, leading to a decrease in its rotational frequency and an expansion of the bar (Hernquist & Weinberg

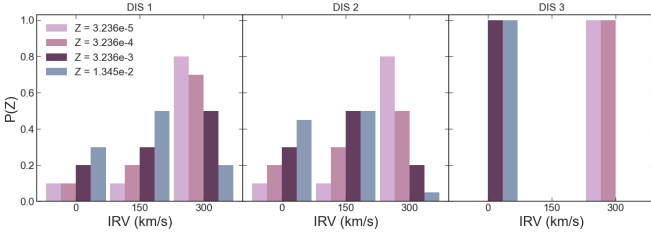


**Fig. 1.** Probability distributions of initial rotational velocities (IRV) for massive stars as a function of the metallicity ( $Z$ ).

1992; Martinez-Valpuesta et al. 2006; Bhattacharjee et al. 2022). As described by Chiba et al. (2021), as the bar decelerates, the resonance regions sweep through the stellar phase-space, capturing and dragging a number of stars. Chiba & Schönrich (2021) estimated an increase in corotation radius,  $R_{\text{cr}}$ , since the formation of the bar (here assumed to have happened 8 Gyr ago) of at least  $\Delta R_{\text{cr}} = 1.6$  kpc. If we assume that the bar also grows by the same fraction, then

$$\Delta R_b = \Delta R_{\text{cr}} \frac{R_b}{R_{\text{cr}}} \simeq 1.2 \text{ kpc}, \quad (2)$$

where  $R_b = 5$  kpc is the bar half-length (Wegg et al. 2015) and  $R_{\text{cr}} = 6.6$  kpc (Chiba & Schönrich 2021; Clarke & Gerhard 2022). The fraction of stellar mass swept away by the growing bar is then

$$f = \frac{2\pi\Delta R_b \times R_b \Sigma(R)}{M_b}, \quad (3)$$

where  $M_b \simeq 10^{10} M_\odot$  is the bar mass (Bland-Hawthorn & Gerhard 2016). Therefore, given a stellar surface mass density predicted by our model at  $R_{\text{GC}} \simeq 5$  kpc of  $\Sigma(5 \text{ kpc}) \simeq 143 M_\odot \text{ pc}^{-2}$ , we can compute the fraction of stellar mass that is trapped by the growing bar at  $\sim 5$  kpc, which is  $f \simeq 53\%$ . This must be considered an upper limit since (i) not all the stars that are trapped into the corotation resonance will also be part of the bar and (ii) only a fraction of stars trapped in the bar will live long enough to populate the Galactic bulge region (which in our model extends until 3 kpc).

From the observational and kinematical point of view, stars that were originally in a disk orbit, will end up in a bar orbit and will then be observed preferentially close to the mid-plane, kinematically colder than MP stars and characterized by ordered orbits. This interpretation is supported by the kinematics of the metal-richest stars in our sample, which we recall is investigated in Rojas-Arriagada et al. (2020). The kinematic of the studied sample agrees well with both the cylindrical rotation pattern predicted by  $N$ -body simulations of bulges formed by secular evolution of the disk through the influence of a forming bar and with observations of external local galaxies with a bar-dominated morphology. The rotation pattern in the sample is also observed to be enhanced toward the mid-plane, which has been interpreted as a signature of a bar-dominated dynamics (see Zhao et al. 1996; Molaeinezhad et al. 2016; Gómez et al. 2018). For a detail discussion about the kinematic of the adopted sample we refer to Rojas-Arriagada et al. (2020).

## 4. Results without accreted stars

In the following sections, we present results for the MDF and the abundance patterns as predicted by models similar to the best one proposed by Matteucci et al. (2019), but with updated yields

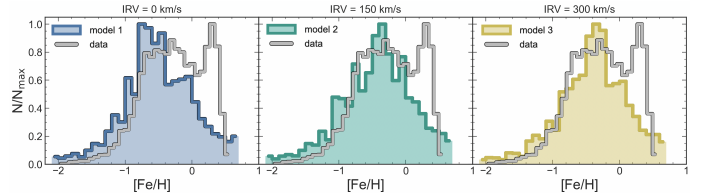


**Fig. 2.** MDFs as predicted by models 1, 2, and 3 obtained with the prescriptions of the best Matteucci et al. (2019) model with yields of rotating massive stars with initial velocities equal to  $0 \text{ km s}^{-1}$  (left panel),  $150 \text{ km s}^{-1}$  (middle panel), and  $300 \text{ km s}^{-1}$  (right panel).

**Table 1.** Input parameters for the chemical evolution models.

Model	IRV	$\delta t_{\text{SF}}$ (Myr)	IMF
Model 1	$0 \text{ km s}^{-1}$ – constant	250	Salpeter
Model 2	$150 \text{ km s}^{-1}$ – constant	250	Salpeter
Model 3	$300 \text{ km s}^{-1}$ – constant	250	Salpeter
Model 4	$0 \text{ km s}^{-1}$ – constant	250	Chabrier
Model 5	$150 \text{ km s}^{-1}$ – constant	250	Chabrier
Model 6	$300 \text{ km s}^{-1}$ – constant	250	Chabrier
Model 7	DIS 1	250	Chabrier
Model 8	DIS 2	250	Chabrier
Model 9	DIS 3	250	Chabrier
Model 4a	$0 \text{ km s}^{-1}$ – constant	0	Chabrier
Model 4b	$0 \text{ km s}^{-1}$ – constant	150	Chabrier
Model 4c	$0 \text{ km s}^{-1}$ – constant	350	Chabrier
Model 8a	DIS 2	0	Chabrier
Model 8b	DIS 2	150	Chabrier
Model 8c	DIS 2	350	Chabrier
Model 9a	DIS 3	0	Chabrier
Model 9b	DIS 3	150	Chabrier
Model 9c	DIS 3	350	Chabrier

**Notes.** The columns respectively provide the name of the model, the initial rotational velocity of massive stars, the duration of the pause in the SF, and the adopted IMF. The first three models are the Matteucci-like ones. We adopted the same prescriptions as the best model from Matteucci et al. (2019), changing only the yields for massive stars. For the remaining models, we adopted either a constant rotational velocity for massive stars or a distribution of rotational velocities (presented in Sect. 3). Different durations ( $\delta_{\text{SF}}$ ) for the quenching of the SF were also tested.

from rotating massive stars, alongside with results obtained from the newly developed models presented in the last section (see Table 1). In this kind of model we assume that the two stellar populations in the bulge (MP and MR) form because of a hiatus in the SF. In Table 1, we report the different models tested in this work. In particular, in the first column we report the name of the model, in the second column the adopted prescriptions for the initial rotational velocity (IRV) of massive stars, in the third column the duration of the quenching in the SF and in the last column the assumed IMF.

### 4.1. Metallicity distribution function

In Fig. 2 we report the results of model 1, model 2, and model 3 obtained with the prescriptions of Matteucci et al. (2019)'s best model but with updated yields for rotating massive stars (see Table 1 for reference). None of the three models is able to reproduce the MDF observed in the new set of observational

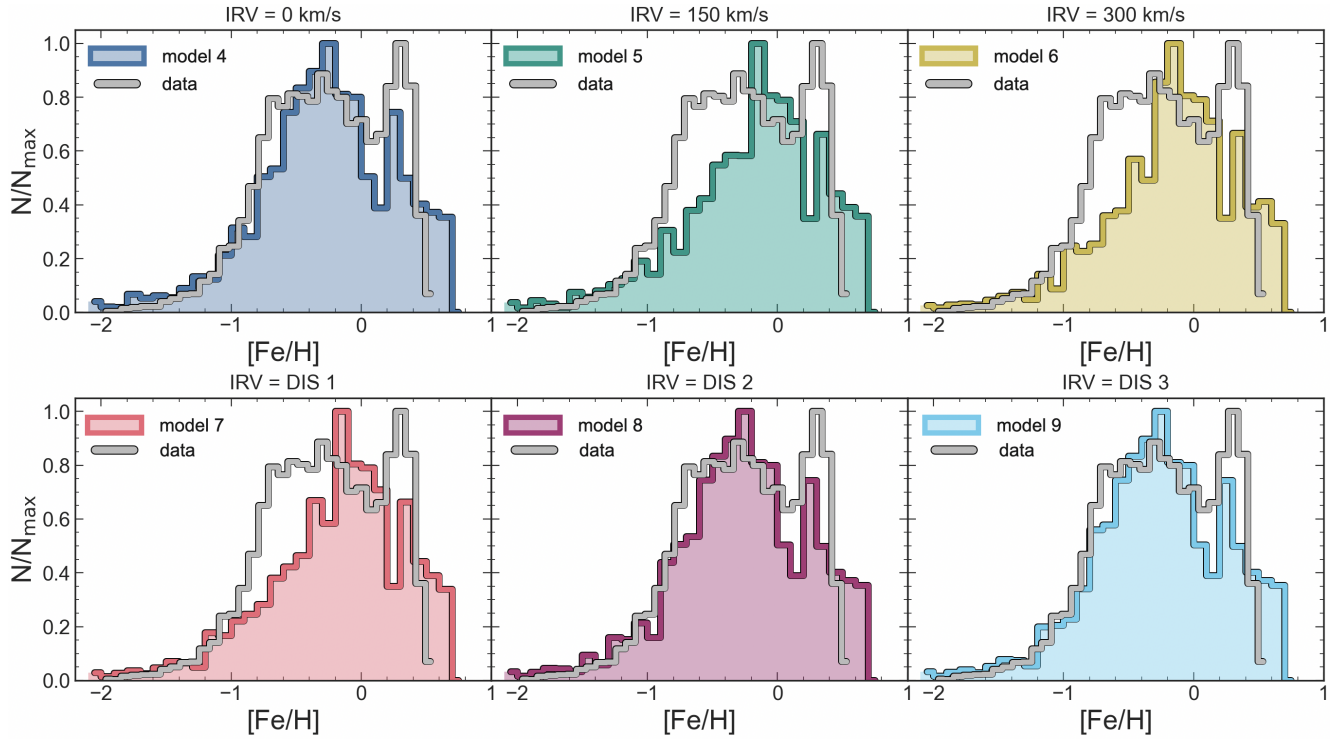


**Fig. 3.** MDFs predicted with a Chabrier IMF and a pause in the SF lasting 250 Myr. The MDFs differ for the different initial rotational velocities adopted. Models 4, 5, and 6 (first row) have constant initial rotational velocities, and models 7, 8 and 9 are characterized by a distribution of the initial rotational velocities (see Table 1).

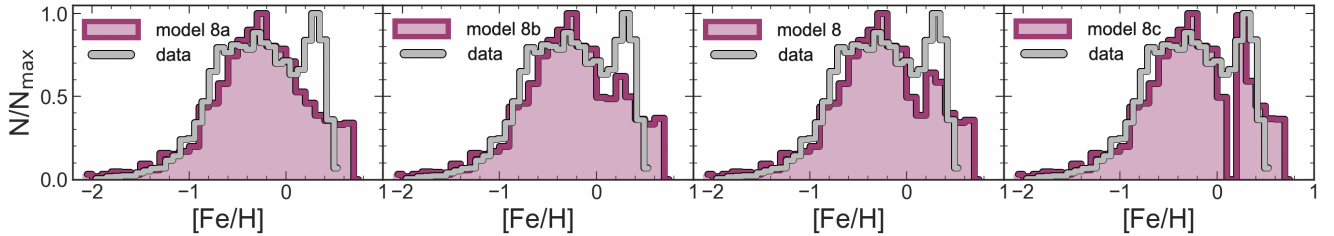


**Fig. 4.** MDFs predicted by models 8(a–c) characterized by different durations of the SF pause (0, 150, 250, and 350 Myr).

data. The predicted MDFs are shifted toward low metallicities, in particular in the case of model M19-0 where the MDF is peaked at  $[Fe/H] \simeq -0.6$  dex. In the case of models 2 and 3 the peak is at higher metallicities, at  $[Fe/H] \simeq -0.3$  dex, since rotation in massive stars increases the production of Fe. However, the observed MR peak is still not reproduced, and, moreover, all of the models overestimate the stars in the low metallicity regime.

In Fig. 3 we present the results of models 4, 5, and 6 in the first row, and of models 7, 8, and 9 in the second row. All the models show an improved agreement with data with respect to old models. Specifically, models 4, 8, and 9 effectively reproduce the positions of the first and second MDF peaks. In contrast, models 5, 6, and 7 show a less good fit with the data, yielding to similar MDF shapes: the MP peak is shifted toward too high metallicities, with a notable underproduction of stars in the intermediate metallicity range ( $-1 \leq [Fe/H] \leq -0.25$  dex).

The drop produced by all of the models between the MP and the MR peak appears to be slightly too deep with respect to the observed one. The depth of the drop in the MDF increases with the duration of the SF pause. This can be seen in Fig. 4,

where we increase the duration of the SF pause from 0 to 150, 250, and 350 Myr (for illustration purposes we show results only for models 8(a–c)). The longer the SF pause lasts, the deeper the drop will get in the MDF and, as a consequence, a higher second peak in the MDF will be obtained. In the time interval during which the SF is quenched, no new SF occurs and the production of Fe slows down because of the lack of new massive stars (Type Ia SNe are still active, and therefore the production of Fe has not completely stopped). While the SF is being quenched, the gas builds up due to the ongoing infall; hence, more gas has accumulated by the end of a longer pause. When the SF resumes, since it is proportional to the gas available in the ISM, it will be stronger after a longer pause, and as a consequence the stellar number density will be larger. This can be seen in Fig. 5, where we report the evolution of the SF,  $[Fe/H]$ , and surface number density of stars as a function of time for pauses in the SF of 150, 250, and 350 Myr. Thus, the height of the MR peak can be modeled by changing the duration of the SF pause or, as recently analyzed by Romano et al. (2023) for the chemical enrichment of the bulge fossil Terzan 5, by removal of a major fraction of the gas left over from the first SF episode.

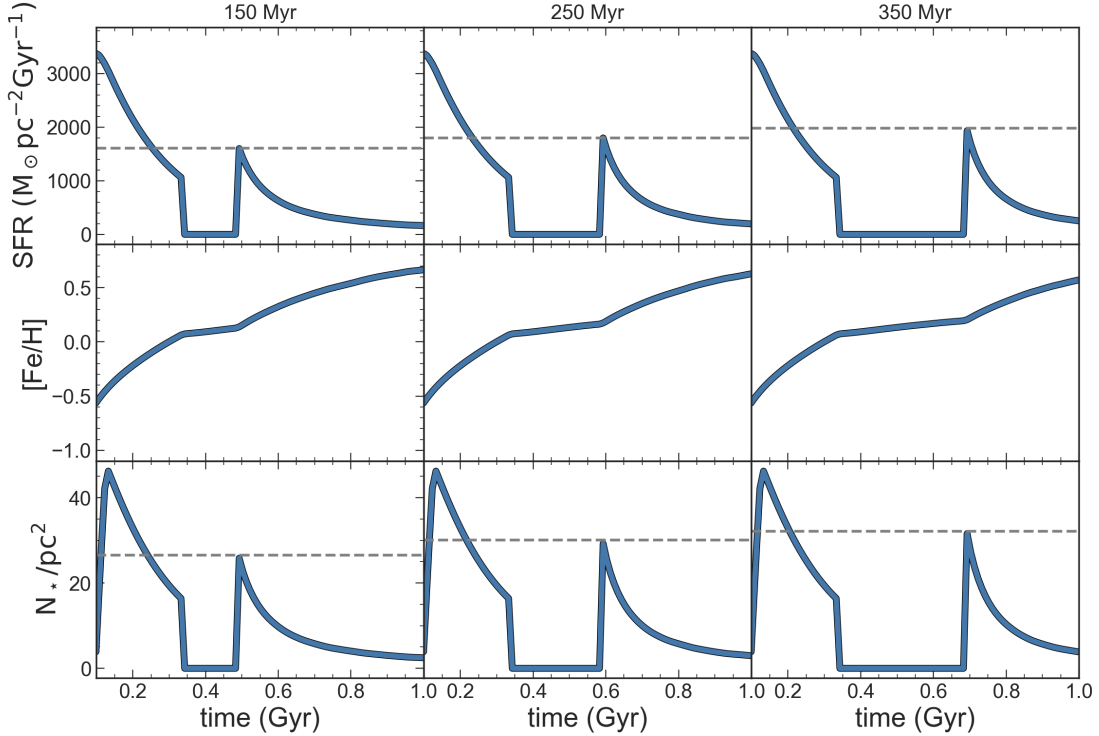


**Fig. 5.** Star formation rate, [Fe/H], and surface number density of stars as a function of time predicted by models 4, 4b, and 4c. The three models differ only in the duration of the SF quenching period.

#### 4.2. Abundance patterns

In Fig. 6 we report the  $[\alpha/\text{Fe}]$  versus  $[\text{Fe}/\text{H}]$  abundance patterns of Mg, O, Al, and Si as predicted by models 4(a–c), 8(a–c), and 9(a–c). Models with a pause in the SF produce a break in the  $[\alpha/\text{Fe}]$  versus  $[\text{Fe}/\text{H}]$  that is also visible in the APOGEE data, which show indeed two overdense regions in correspondence of  $[\text{Fe}/\text{H}] \approx -0.5$  dex and  $[\text{Fe}/\text{H}] \approx 0.25$  dex. The break in the abundance patterns occurs because the pause in the SF causes cessation of  $\alpha$ -element production in massive stars, while the Fe production continues (even if it is significantly slowed) thanks to Type Ia SNe and their longer time-delays. The bimodal distribution that is present in the set of data used in this work is also reported by Queiroz et al. (2021, see also Rojas-Arriagada et al. 2019; Queiroz et al. 2020), although in their case the depression between the two peaks seems to be more pronounced, and the two sequences are more noticeably distinct. However, the different datasets are comparable and their differences are not affecting our conclusions.

Rotation in massive stars increases the production of O, Al, and Si, while it reduces that of Mg. Since the theoretical distributions of rotational velocities differ mainly at low metallicities, this effect is visible only for  $[\text{Fe}/\text{H}] \leq -1$  dex. All the models are underestimating the  $[\text{Mg-Al}/\text{Fe}]$  versus  $[\text{Fe}/\text{H}]$  trends and overestimating the  $[\text{Si}/\text{Fe}]$  one. Models C-0(A-D) are those that best reproduce the  $[\text{Al}/\text{Fe}]$  versus  $[\text{Fe}/\text{H}]$  as well as the  $[\text{O}/\text{Fe}]$  versus  $[\text{Fe}/\text{H}]$ , even if deviations at low metallicities are present. The general trend of the observed abundance ratios is, however, well reproduced by models 4(a–c), in particular with a pause of 250 Myr. Deviations from the observed pattern are therefore due to the adopted set of yields, the IMF, or a combination of the two. A Salpeter (1955) IMF would indeed predict lower abundance patterns for the  $\alpha$  elements, because of a lower production of massive stars. Therefore, by keeping the same set of yields, this

would improve the agreement with the  $[\text{O}/\text{Fe}]$  and  $[\text{Si}/\text{Fe}]$  versus  $[\text{Fe}/\text{H}]$  trends but, at the same time, would worsen the ones with the  $[\text{Mg}/\text{Fe}]$  and  $[\text{Al}/\text{Fe}]$  as well as with the MDF (as shown in the previous section). Concerning the yields variations, adopting the set of Kobayashi et al. (2006, which accounts for mass loss but not rotation) produces the results shown in Fig. 7 for both a Salpeter (1955) and a Chabrier (2003) IMF. The  $[\text{Mg}/\text{Fe}]$  versus  $[\text{Fe}/\text{H}]$  trend is improved with respect to model 4, in particular by adopting a Salpeter (1955) IMF (see Matteucci et al. 2019). However, O, Al and Si the fit with the data is poorly improved or gets even worse. If the assumption of a Chabrier (2003) is valid, then corrections to the Limongi & Chieffi (2018) yields must be applied. According to our model, the production of Mg and Al should be increased by a factor of  $\sim 1.5$ , while that of Si should be decreased by a factor of  $\sim 0.7$ . When those corrections are applied, the derived results for the  $[\text{Mg-Al-Si}/\text{Fe}]$  abundance patterns are those shown in Fig. 8 as a function of both the  $[\text{Fe}/\text{H}]$  and the number of stars produced. In this way, it is possible to better appreciate the decrease in the stellar density that is produced by our model at  $0.0 \leq [\text{Fe}/\text{H}] \leq 0.2$ , compatible with the observed data.

In Fig. 9 we report results of models 4(a–c), 8(a–c) and 9(a–c) for the  $[\text{Ce}/\text{Fe}]$  versus  $[\text{Fe}/\text{H}]$  abundance pattern. The characteristic “banana” shape of  $s$ -process elements can be seen in the data at  $-0.77 \leq [\text{Fe}/\text{H}] \leq 0.60$  dex. At lower  $[\text{Fe}/\text{H}]$ , dispersion in the data is also present with mean value  $[\text{Ce}/\text{Fe}] \approx 0.20$  dex. The bimodal distribution clearly seen in the  $\alpha$  elements is less evident for Ce. This can be due both to the larger scatter observed in the Ce abundance pattern and, most importantly, to the fact that Ce is also produced by LIMSS (its  $s$ -process component) and by MNSs (its  $r$ -process component), and therefore its production will continue even if a quenching in the SF is present. Indeed, in the model results as well, the different duration of the SF pause has very little impact on the overall  $[\text{Ce}/\text{Fe}]$

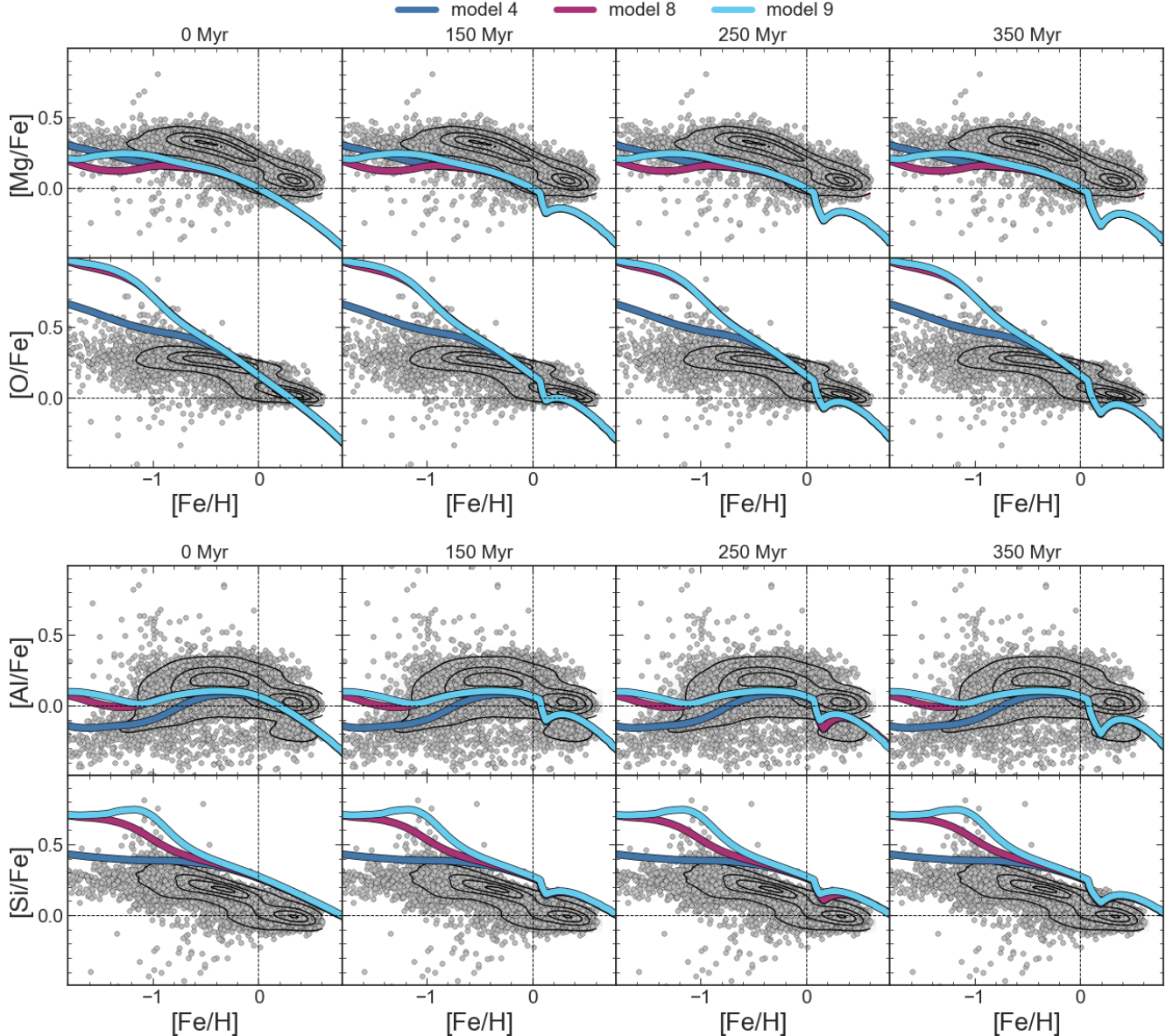


**Fig. 6.** Predicted  $[{\rm Mg}/\text{Fe}]$ ,  $[{\rm O}/\text{Fe}]$ ,  $[{\rm Al}/\text{Fe}]$ , and  $[{\rm Si}/\text{Fe}]$  vs.  $[\text{Fe}/\text{H}]$  trends for models 4(a–c), 8(a–c), and 9(a–c) without the contribution from accreted disk stars. The models differ in the prescriptions on the initial rotational velocities of massive stars and the duration of the SF quenching period (see Table 1).

versus  $[\text{Fe}/\text{H}]$  pattern, without affecting too much the comparison with the data. For the  $s$ -process elements, such as Ce, rotation in massive stars increases their production, especially at low metallicities. As already discussed in Molero et al. (2023), it is possible to note the strong effect of the magneto-rotational SNe at low metallicities responsible for the creation of the plateau visible in models 4(a–c). When higher rotational velocities for massive stars are considered, their contribution dominates at low  $[\text{Fe}/\text{H}]$ . However, because of such high velocities, models 9(a–c) are overproducing the  $[{\rm Ce}/\text{Fe}]$  versus  $[\text{Fe}/\text{H}]$  at low  $[\text{Fe}/\text{H}]$ , while models 4(a–c) and 8(a–c) are more in agreement with the data. At higher  $[\text{Fe}/\text{H}]$ , LIMSSs dominate the production of  $s$ -process elements, creating a bump in the  $[{\rm Ce}/\text{Fe}]$ . With the adopted sets of yields, however, the production of Ce from LIMSSs is too strong, and it should be reduced of at least a factor of 3 in order to have a better agreement with the data, as shown by the dashed purple line in the figure, corresponding to models 4(a–c), but with reduced AGB yields.

## 5. Results with accreted stars

As discussed in Sect. 1, in this work we are testing the hypothesis put forward by Matteucci et al. (2019), according to which the MR peak of the Galactic bulge is due to both stars that are formed in situ and to stars that formed in the innermost part of the Galactic disk and got trapped in the Galactic bar. This is also supported by the MDF of the innermost part of the Galactic disk obtained by our model, which presents a peak at a similar value of  $[\text{Fe}/\text{H}]$  to that for the MR population in the bulge. This is shown in Fig. 3 of Matteucci et al. (2019), where the adopted model for the disk is the one-infall model of Grisoni et al. (2017) with a constant SF efficiency of  $1 \text{ Gyr}^{-1}$ , a Kroupa et al. (1993) IMF and nucleosynthesis prescriptions from Romano et al. (2010). Here, for consistency with our previous more recent works, we used the delayed two-infall model presented by Palla et al. (2020) and adopted by Molero et al. (2023) to model the evolution of

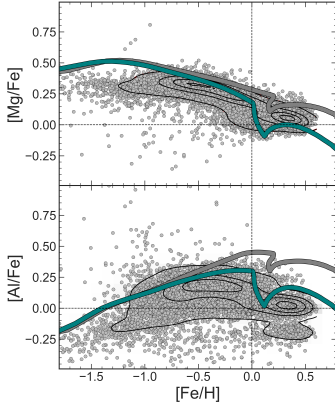


**Fig. 7.** Predicted  $[\text{Mg}/\text{Fe}]$ ,  $[\text{O}/\text{Fe}]$ ,  $[\text{Al}/\text{Fe}]$ , and  $[\text{Si}/\text{Fe}]$  vs.  $[\text{Fe}/\text{H}]$  trends for model 4 but with yields set for massive stars from Kobayashi et al. (2006) and different IMFs.

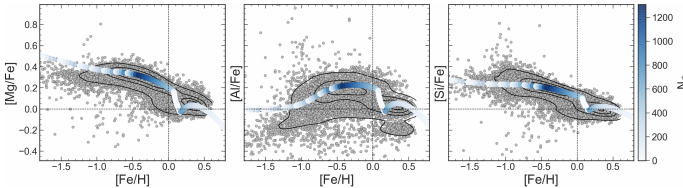


**Fig. 8.** Predicted  $[\text{Mg}/\text{Fe}]$ ,  $[\text{Al}/\text{Fe}]$ , and  $[\text{Si}/\text{Fe}]$  vs.  $[\text{Fe}/\text{H}]$  trends for model 4 with corrected yields for massive stars.

several neutron-capture elements in the MW disk (see also Spitoni et al. 2019, 2021). At variance with the Grisoni et al. (2017) model, we adopted a higher SF efficiency of  $9 \text{ Gyr}^{-1}$  (as opposed to  $1 \text{ Gyr}^{-1}$ ) in the inner region of the disk, as suggested by Colavitti et al. (2009, see also Spitoni et al. 2015). The nucleosynthesis prescriptions are from Molero et al. (2023) best model and a Kroupa et al. (1993) IMF is adopted.

### 5.1. Metallicity distribution function

In Fig. 10 we present the results of models 4(a–c) for the MDF, with the contribution of stars from the inner disk. To account for the fraction of stars, initially calculated as an upper limit in Sect. 3, we performed tests with different values, namely  $f = 10, 20, 30, 40\%$ . As shown in the first row of the figure, when we do not consider any pause in SF, the inclusion of a certain percentage of stars from the Galactic disk alone does not suffice to replicate the MR peak observed in the MDF. However, by assuming a SF pause of 150 Myr leads to an improved agreement with the data. Model 4, with a 250 Myr SF pause and  $f = 40\%$  stars from the inner disk, best reproduces the observed results. Both the MP and the MR peaks within the MDF are notably well matched, not only in terms of their positions but also in terms of their relative heights. The model, however, still produces a slightly deeper hole between the two peaks, as well as an overproduction of star for  $[\text{Fe}/\text{H}] \geq 0.5$  dex. This two issues are nicely solved by performing a convolution between the distribution predicted by our model 4 with a normal distribution with  $\sigma = 0.1$  dex. In fact, as shown in Fig. 11, the two discrepancies are well inside the uncertainties of the model and data.

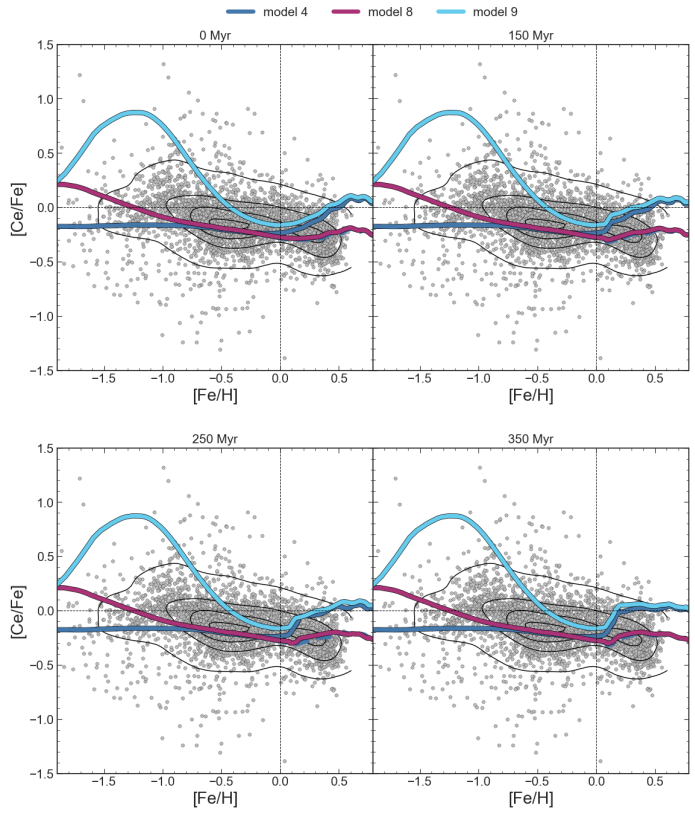


**Fig. 9.** Same as Fig. 6 but for Ce. The dashed purple line corresponds to model 8 but with reduced yields from LIMSS.

### 5.2. Abundance patterns

In Fig. 12 we report results for the  $[\alpha/\text{Fe}]$  versus  $[\text{Fe}/\text{H}]$  abundance patterns. The blue lines in the diagrams refer to the chemical enrichment of stars born in situ in the bulge, while the red lines refer to stars born in the inner disk of the MW and then accreted by the growing bar. The contribution from the accreted population appears in the  $[\alpha/\text{Fe}]$  versus  $[\text{Fe}/\text{H}]$  diagrams from  $[\text{Fe}/\text{H}] \simeq +0.2$  dex, which corresponds to the value of metallicity at which the bulge starts growing the bar. This value of metallicity is in agreement with the position of the MR cluster of data in the  $\alpha$ -element abundance patterns and is obtained by assuming that the bar age is  $\sim 8$  Gyr, namely that the accretion of stars from the inner disk started  $\sim 5.5$  Gyr ago. The stars being accreted will enrich the ISM in the bulge region with the product of their chemical composition, which will reflect that of the location where they were trapped. Therefore, according to the time-delay model (see Matteucci 2012), we expect their abundance patterns to lie below that due to the stellar population born in situ in the bulge, as shown in the figure. The abundance patterns predicted by our model for the accreted population is well in agreement with the bulge MR data for  $[\text{Al}/\text{Fe}]$  and for  $[\text{Si}/\text{Fe}]$  versus  $[\text{Fe}/\text{H}]$ , but underproduce data for  $[\text{Mg}/\text{Fe}]$  and for  $[\text{O}/\text{Fe}]$  versus  $[\text{Fe}/\text{H}]$ . This can potentially be due to the adopted IMF for modeling the inner MW disk, here namely a Kroupa et al. (1993) IMF. Among the different IMFs, the Kroupa et al. (1993) IMF is the one that guarantees good fits to the observed properties of the solar neighborhood (see Romano et al. 2005). In chemical evolution studies, this parametrization for the IMF is commonly adopted not only for the solar vicinity, but also for modeling the all MW disk. However, there is currently no strong observational evidence that the Kroupa et al. (1993) IMF provides the

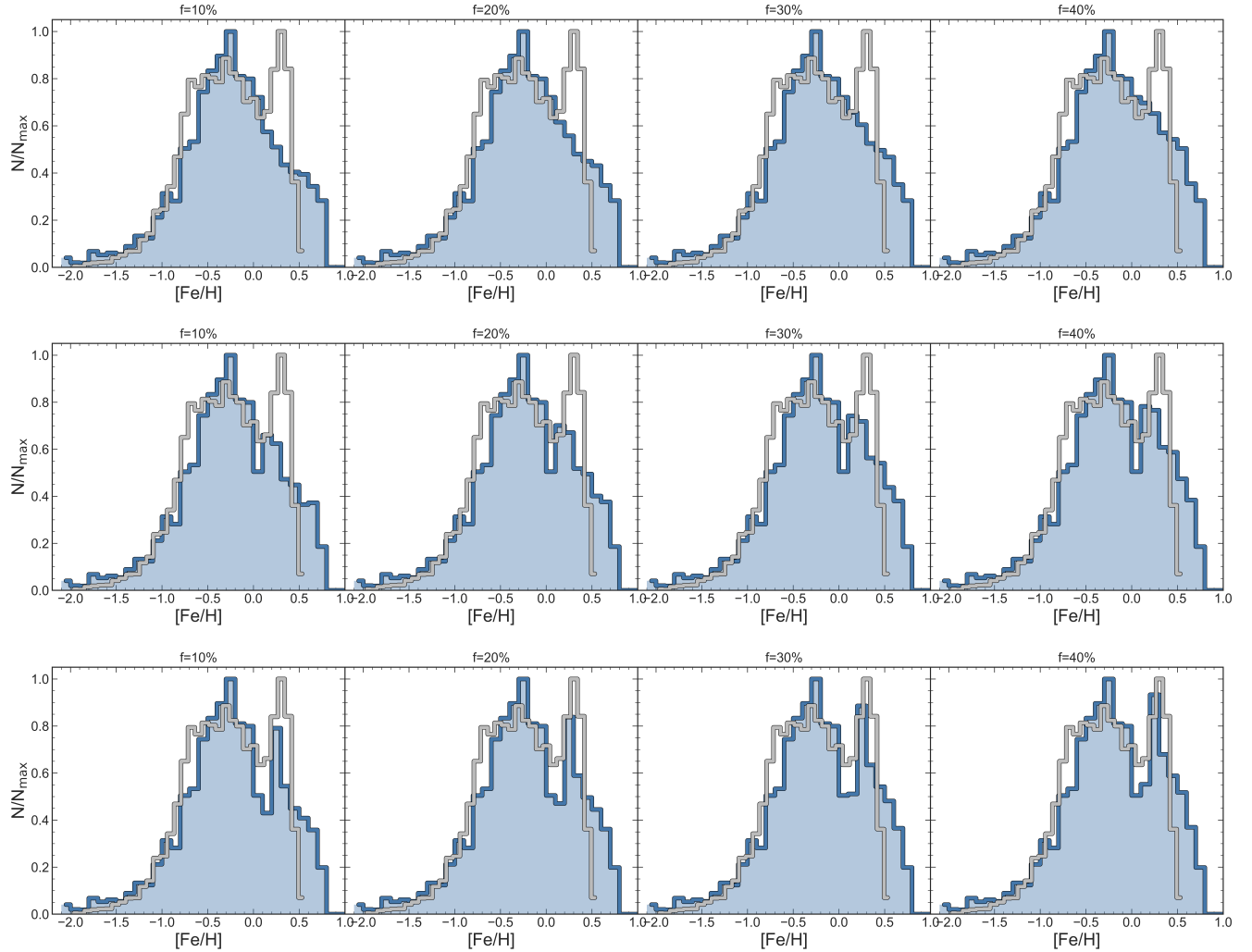


**Fig. 10.** MDF of the Galactic bulge predicted by models 4, 4a, and 4b with no pause in the SF (first row), 150 Myr of pause (second row), and 250 Myr (third row, model 4) and with different fractions of inner disk stars contributing to the bar.

best fit with the inner MW disk as well. It is reasonable to presume that, moving outward in radius from the Galactic bulge toward the inner disk and the solar neighborhood, the slope of the IMF may get steeper. So that, if a Chabrier (2003) IMF can be adopted for the Galactic bulge (as shown in the previous sections) and a Kroupa et al. (1993) is ideal for the MW disk around  $R_{\text{GC}} \sim 8$  kpc, then a Salpeter (1955) IMF may be the right one to model the innermost part of the MW disk.

## 6. Discussion and conclusions

Our model of the Galactic bulge is based on the model from Matteucci et al. (2019), and it is mainly constrained to the shape of the bulge MDF as observed in the sample of  $\sim 13\,000$  giant stars from APOGEE DR16 (Rojas-Arriagada et al. 2020). Our main assumption is that the MW bulge was formed by a strong SF episode, triggered by a fast collapse of primordial gas, which is mainly responsible for the creation of the MP population observed in the MDF as well as in the  $[\alpha/\text{Fe}]$  versus  $[\text{Fe}/\text{H}]$  abundance patterns. A second, smaller burst of SF and an accretion of disk stars from the Galactic bar are assumed to be responsible for the creation of the MR stellar population. Our main conclusions are the following:

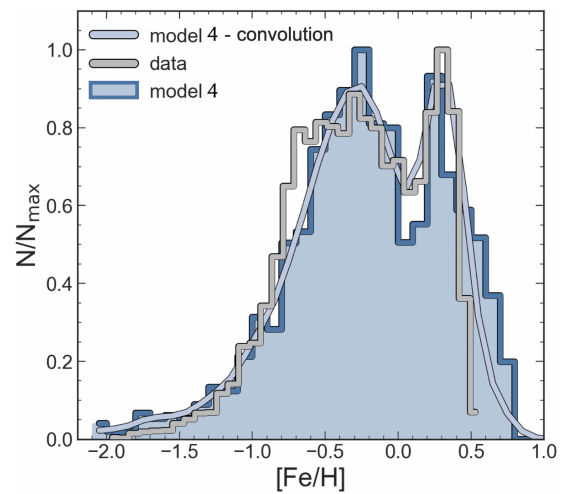


**Fig. 11.** MDF of the Galactic bulge as predicted by model 4 with a fraction of 40% of stars from the inner disk. The model has been convoluted with a normal distribution with  $\sigma = 0.1$  dex to conservatively take the spectroscopic uncertainly in metallicity into account.

- The best Matteucci et al. (2019) model, which assumes a delay between the two SF bursts of 250 Myr, is not able to

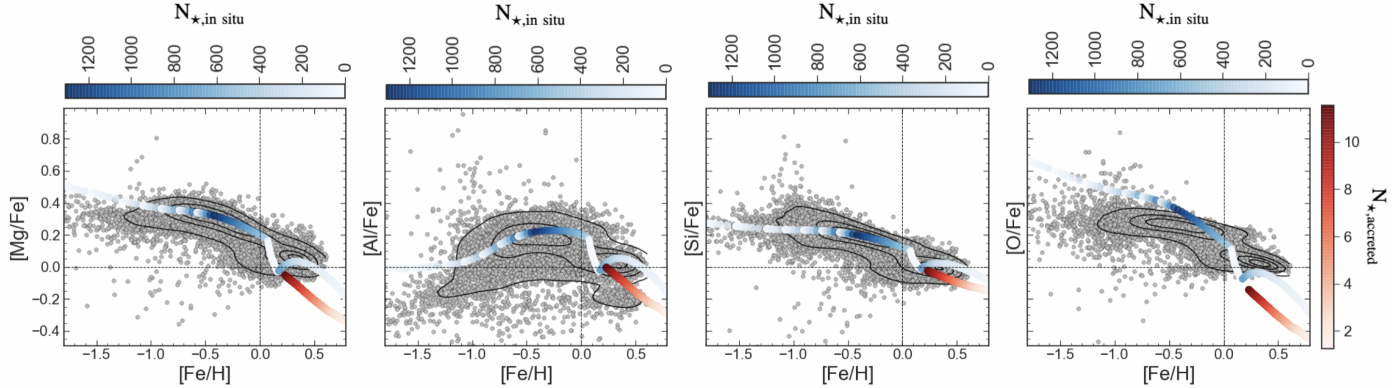


**Fig. 12.**  $[\alpha/\text{Fe}]$  versus  $[\text{Fe}/\text{H}]$  abundance patterns for Mg, Al, Si, and O as predicted by model 4 (upper blue lines) responsible for the creation of the in situ stellar population and by stars from the inner disk (lower red lines) responsible for the creation of the accreted stellar population in the bulge. Lines are color-coded by the number of stars formed by the model, with the upper blue colorbar referring to the in situ population and the right red colorbar referring to the accreted population.

reproduce the observed MDF of the bulge represented by the Rojas-Arriagada et al. (2020) dataset if yields for rotating massive stars from Limongi & Chieffi (2018) are used together with a Salpeter (1955) IMF.

- By adopting a Chabrier (2003) IMF, rather than a Salpeter (1955) one, the agreement between the Matteucci et al. (2019) model and the data is improved. In particular, a model that assumes no rotational velocity for massive stars or a distribution of rotational velocities that favors slow rotation at the present time best reproduces the observed MDF.
- The observed abundance trends of  $\alpha$  elements are well reproduced with a delay between the two SF bursts of 250 Myr, but all the models underproduce the  $[\text{Mg}/\text{Fe}]$  and  $[\text{Al}/\text{Fe}]$  versus  $[\text{Fe}/\text{H}]$  relations and overproduce the  $[\text{Si}/\text{Fe}]$  one. The situation is slightly improved by using a different set of yields (the one from Kobayashi et al. 2006), but only in the case of Mg. We conclude that, if the assumption of a Chabrier (2003) IMF is valid, then corrections need to be applied to the Limongi & Chieffi (2018) set of yields (R). The production of Mg and Al should be increased by a factor of  $\sim 1.5$ , while that of Si should be decreased by a factor of  $\sim 0.7$ .
- A model with no massive star rotation also best reproduces the  $[\text{Ce}/\text{Fe}]$  versus  $[\text{Fe}/\text{H}]$  trend, mainly because of the contribution from magneto-rotational SNe at low metallicities. However, the abundance ratios are overestimated at high  $[\text{Fe}/\text{H}]$  because of the overly strong impact of AGB stars, whose contribution to  $s$ -process element nucleosynthesis, in agreement with other chemical evolution studies (e.g., Rizzuti et al. 2019, 2021; Molero et al. 2023), should be decreased by at least a factor of 2.
- To reproduce the MR peak of the MDF, we estimate that at least  $\sim 40\%$  of stars should get trapped by the growing bar. However, if no pause in the SF is assumed, contamination of stars from the inner disk is not sufficient to fully reproduce the MR peak of the MDF; therefore, a pause in the SF of 250 Myr must be considered.
- The accreted population from the innermost part of the disk is able to fit the MR data relative to the  $[\alpha/\text{Fe}]$  versus  $[\text{Fe}/\text{H}]$  diagrams in the case of Al and Si, but it underproduces the abundances for Mg and O. We suggest that this can be reconciled by adopting a steeper IMF.

In summary, to fit the bimodal shape of the bulge MDF, one of the main assumptions of our model is a two-phase SF history consisting of an initial starburst followed by a quenching

episode and a second, less intense burst. During the first burst, the MP and high- $\alpha$  bulge stars are formed. In particular, the rapid SF cessation process appears critical for reproducing the observed alpha bimodality as well as the well-defined depression between the two MDF peaks (see also Lian et al. 2020, 2021). Simulations of MW mass halos suggest that the gas infall rate peaks around redshift  $z = 2$  and then declines (see, e.g., van de Voort et al. 2011; Woods et al. 2014). After the peak, the MW inevitably starts quenching its SF (see also Haywood et al. 2016). According to Haywood et al. (2018), even if the decline in the gas infall rate coincides with the quenching in the SF, it is not necessarily its main cause. In fact, in their model, there is still gas in the MW disk during this epoch, as has been observed in MW-type galaxies at redshifts around  $z = 1.5$  (Daddi et al. 2010). As a consequence, even if a decline in the infall rate might have contributed to the SF quenching, it is not necessarily its main (or unique) cause.  $N$ -body hydrodynamic simulations from Khoperskov et al. (2018) show that it is possible for the bar to suppress the SF. In their simulations, they quantitatively explore the relation between bar formation and SF in gas-rich galaxies and conclude that the action of a stellar bar efficiently quenches the SF, reducing its rate by a factor of 10 in less than 1 Gyr. The SF efficiency decreases and, in all of their models, the bar quenches the SF in the galaxy. Similarly, Haywood et al. (2016) propose that in the MW the action of the bar could have increased the gas turbulence, stabilizing the disk against SF and quenching its SF. As a consequence, the suppression of the SF is not associated with a substantial consumption of the available gas. The gas would still be present in the disk, but its high turbulence would significantly limit the SF efficiency. However, it must be noted that in order to fit the two peaks in the observed MDF, the quenching in the SF would have to happen at earlier times with respect to the formation of the bar. As a consequence, the most plausible explanation would be that the first, strong burst of SF consumed the majority of the available gas, causing the quenching. However, since during the quenching phase the infall of primordial gas is still active, the gas is accumulated until it triggers a second, less intense burst of SF.

We also stress that our model does not take the contribution from stars from the halo into account, nor accreted globular cluster debris or dwarf galaxies (see, e.g., Fernández-Trincado et al. 2021). However, conclusions from our work do not necessarily exclude contributions from other astrophysical environments to the chemical enrichment of the Galactic bulge. Indeed, as

underlined in the Introduction, the Galactic bulge formation mechanism is most probably a combination of different processes. These processes might include not only strong gas accretion together with secular processes, but also major and/or minor mergers. We are inclined to think that possible contributions from small satellite galaxies and/or part of the stellar halo would not change our general conclusions. In support of this hypothesis, Portail et al. (2017) conclude that only part of the very MP region of the MDF is due to the inner part of the stellar halo. If that is the case, this would influence the shape of the first peak of the MDF predicted by our model, which would suggest a less strong first SF episode; however, our conclusions on the fraction of stars that are trapped by the bar and yields from massive stars would remain unaffected. Moreover, the  $[\alpha/\text{Fe}]$  and the metallicity content of those stars are generally lower than the bulk of bulge stars, and as a consequence, their influence on the chemical evolution should be minimal. In particular, according to the Chemical Origins of Metal-poor Bulge Stars (COMBS), the MP bulge has higher levels of Ca and a lower dispersion in the  $\alpha$ -element abundances compared to halo stars of the same metallicity (see Lucey et al. 2019). Similarly, high neutron-capture abundance stars are found at a much lower rate in the bulge than in the halo or in MP dwarf spheroidal galaxies, and their abundance peculiarities in neutron-capture elements can often be justified with combinations of several nucleosynthetic processes (see Koch et al. 2016, 2019).

**Acknowledgements.** M. Molero thanks Rimpei Chiba and Mattia Sormani for the very useful discussions and suggestions concerning bar dynamics. M. Molero thanks Marco Limongi for interesting discussions concerning stellar rotation. F. Matteucci thanks I.N.A.F. for the 1.05.12.06.05 Theory Grant – Galactic archaeology with radioactive and stable nuclei. A.R.A. acknowledges support from DICYT through grant 062319RA. This research was partially supported by the Munich Institute for Astro-, Particle and BioPhysics (MIAPbP) which is funded by the Deutsche Forschungsgemeinschaft (DFG, German Research Foundation) under Germany’s Excellence Strategy–EXC-2094–390783311. This work was supported by the Deutsche Forschungsgemeinschaft (DFG, German Research Foundation)-Project-ID 279384907-SFB 1245, the State of Hessen within the Research Cluster ELEMENTS (Project ID 500/10.006).

## References

- Abadi, M. G., Navarro, J. F., Steinmetz, M., & Eke, V. R. 2003a, *ApJ*, **591**, 499  
 Abadi, M. G., Navarro, J. F., Steinmetz, M., & Eke, V. R. 2003b, *ApJ*, **597**, 21  
 Anderson, L. D., Sormani, M. C., Ginsburg, A., et al. 2020, *ApJ*, **901**, 51  
 Athanassoula, E. 2005, *Celest. Mech. Dyn. Astron.*, **91**, 9  
 Baba, J., & Kawata, D. 2020, *MNRAS*, **492**, 4500  
 Babusiaux, C., Gómez, A., Hill, V., et al. 2010, *A&A*, **519**, A77  
 Ballero, S. K., Matteucci, F., Origlia, L., & Rich, R. M. 2007, *A&A*, **467**, 123  
 Barbuy, B., Chiappini, C., & Gerhard, O. 2018, *ARA&A*, **56**, 223  
 Baugh, C. M., Cole, S., & Frenk, C. S. 1996, *MNRAS*, **283**, 1361  
 Bensby, T., Adén, D., Meléndez, J., et al. 2011, *A&A*, **533**, A134  
 Bhattarai, B., Hunt, J., Pearson, S., et al. 2022, *AAS/Division of Dynamical Astronomy Meeting*, **54**, 400.03  
 Binney, J., Gerhard, O. E., Stark, A. A., Bally, J., & Uchida, K. I. 1991, *MNRAS*, **252**, 210  
 Bissantz, N., & Gerhard, O. 2002, *MNRAS*, **330**, 591  
 Bland-Hawthorn, J., & Gerhard, O. 2016, *ARA&A*, **54**, 529  
 Cescutti, G., & Matteucci, F. 2011, *A&A*, **525**, A126  
 Chabrier, G. 2003, *PASP*, **115**, 763  
 Chiappini, C., Matteucci, F., & Romano, D. 2001, *ApJ*, **554**, 1044  
 Chiappini, C., Frischknecht, U., Meynet, G., et al. 2011, *Nature*, **472**, 454  
 Chiba, R., & Schönrich, R. 2021, *MNRAS*, **505**, 2412  
 Chiba, R., & Schönrich, R. 2022, *MNRAS*, **513**, 768  
 Chiba, R., Friske, J. K. S., & Schönrich, R. 2021, *MNRAS*, **500**, 4710  
 Ciambur, B. C., Frakoudi, F., Khoperskov, S., Di Matteo, P., & Combes, F. 2021, *MNRAS*, **503**, 2203  
 Clarke, J. P., & Gerhard, O. 2022, *MNRAS*, **512**, 2171  
 Colavitti, E., Cescutti, G., Matteucci, F., & Murante, G. 2009, *A&A*, **496**, 429  
 Cole, A. A., & Weinberg, M. D. 2002, *ApJ*, **574**, L43  
 Combes, F., Debbasch, F., Friedli, D., & Pfenniger, D. 1990, *A&A*, **233**, 82  
 Cristallo, S., Straniero, O., Gallino, R., et al. 2009, *ApJ*, **696**, 797  
 Cristallo, S., Piersanti, L., Straniero, O., et al. 2011, *ApJS*, **197**, 17  
 Cristallo, S., Straniero, O., Piersanti, L., & Gobrecht, D. 2015, *ApJS*, **219**, 40  
 Daddi, E., Bournaud, F., Walter, F., et al. 2010, *ApJ*, **713**, 686  
 Debattista, V. P., & Sellwood, J. A. 2000, *ApJ*, **543**, 704  
 Fernández-Trincado, J. G., Beers, T. C., Queiroz, A. B. A., et al. 2021, *ApJ*, **918**, L37  
 Freeman, K., Ness, M., Wylie-de-Boer, E., et al. 2013, *MNRAS*, **428**, 3660  
 Frischknecht, U., Hirschi, R., Pignatari, M., et al. 2016, *MNRAS*, **456**, 1803  
 García Pérez, A. E., Allende Prieto, C., Holtzman, J. A., et al. 2016, *AJ*, **151**, 144  
 Ghosh, S., Frakoudi, F., Di Matteo, P., & Saha, K. 2023, *A&A*, **674**, A128  
 Gilmore, G., Randich, S., Asplund, M., et al. 2012, *The Messenger*, **147**, 25  
 Gómez, A., Di Matteo, P., Schultheis, M., et al. 2018, *A&A*, **615**, A100  
 Gonzalez, O. A., Zoccali, M., Vasquez, S., et al. 2015, *A&A*, **584**, A46  
 Grady, J., Belokurov, V., & Evans, N. W. 2020, *MNRAS*, **492**, 3128  
 Grieco, V., Matteucci, F., Pipino, A., & Cescutti, G. 2012a, *A&A*, **548**, A60  
 Grieco, V., Matteucci, F., Meynet, G., et al. 2012b, *MNRAS*, **423**, 3049  
 Grieco, V., Matteucci, F., Ryde, N., Schultheis, M., & Uttenthaler, S. 2015, *MNRAS*, **450**, 2094  
 Grisoni, V., Spitoni, E., Matteucci, F., et al. 2017, *MNRAS*, **472**, 3637  
 Haywood, M., Lehnert, M. D., Di Matteo, P., et al. 2016, *A&A*, **589**, A66  
 Haywood, M., Di Matteo, P., Lehnert, M., et al. 2018, *A&A*, **618**, A78  
 Hernquist, L., & Weinberg, M. D. 1992, *ApJ*, **400**, 80  
 Hill, V., Lecurer, A., Gómez, A., et al. 2011, *A&A*, **534**, A80  
 Hunter, I., Lennon, D. J., Dufton, P. L., et al. 2008, *A&A*, **479**, 541  
 Iwamoto, K., Brachwitz, F., Nomoto, K., et al. 1999, *ApJS*, **125**, 439  
 Johnson, C. I., Rich, R. M., Kobayashi, C., Kunder, A., & Koch, A. 2014, *AJ*, **148**, 67  
 Johnson, C. I., Rich, R. M., Young, M. D., et al. 2020, *MNRAS*, **499**, 2357  
 Johnson, C. I., Rich, R. M., Simion, I. T., et al. 2022, *MNRAS*, **515**, 1469  
 Kennicutt, R. C. 1998, *ApJ*, **498**, 541  
 Khoperskov, S., Haywood, M., Di Matteo, P., Lehnert, M. D., & Combes, F. 2018, *A&A*, **609**, A60  
 Klencki, J., Nelemans, G., Istrate, A. G., & Pols, O. 2020, *A&A*, **638**, A55  
 Kobayashi, C., Umeda, H., Nomoto, K., Tominaga, N., & Ohkubo, T. 2006, *ApJ*, **653**, 1145  
 Koch, A., McWilliam, A., Preston, G. W., & Thompson, I. B. 2016, *A&A*, **587**, A124  
 Koch, A., Reichert, M., Hansen, C. J., et al. 2019, *A&A*, **622**, A159  
 Kraljic, K., Bournaud, F., & Martig, M. 2012, *ApJ*, **757**, 60  
 Kroupa, P., Tout, C. A., & Gilmore, G. 1993, *MNRAS*, **262**, 545  
 Kunder, A., Koch, A., Rich, R. M., et al. 2012, *AJ*, **143**, 57  
 Lian, J., Zasowski, G., Hasselquist, S., et al. 2020, *MNRAS*, **497**, 3557  
 Lian, J., Zasowski, G., Hasselquist, S., et al. 2021, *MNRAS*, **500**, 282  
 Limongi, M., & Chieffi, A. 2018, *ApJS*, **237**, 13  
 López-Corredoira, M., Cabrera-Lavers, A., & Gerhard, O. E. 2005, *A&A*, **439**, 107  
 Lucey, M., Hawkins, K., Ness, M., et al. 2019, *MNRAS*, **488**, 2283  
 Majewski, S. R., Schiavon, R. P., Frinchaboy, P. M., et al. 2017, *AJ*, **154**, 94  
 Martayan, C., Floquet, M., Hubert, A. M., et al. 2007a, *A&A*, **472**, 577  
 Martayan, C., Frémat, Y., Hubert, A. M., et al. 2007b, *A&A*, **462**, 683  
 Martinez-Valpuesta, I., Shlosman, I., & Heller, C. 2006, *ApJ*, **637**, 214  
 Matteucci, F. 2012, *Chemical Evolution of Galaxies* (Berlin, Heidelberg: Springer-Verlag)  
 Matteucci, F., & Brocato, E. 1990, *ApJ*, **365**, 539  
 Matteucci, F., Grisoni, V., Spitoni, E., et al. 2019, *MNRAS*, **487**, 5363  
 McWilliam, A., & Rich, R. M. 1994, *ApJS*, **91**, 749  
 McWilliam, A., & Zoccali, M. 2010, *ApJ*, **724**, 1491  
 Minchev, I., Chiappini, C., & Martig, M. 2016, *Astron. Nachr.*, **337**, 944  
 Minniti, D., Lucas, P. W., Emerson, J. P., et al. 2010, *New Astron.*, **15**, 433  
 Molaeinezhad, A., Falcón-Barroso, J., Martínez-Valpuesta, I., et al. 2016, *MNRAS*, **456**, 692  
 Molero, M., Romano, D., Reichert, M., et al. 2021, *MNRAS*, **505**, 2913  
 Molero, M., Magrini, L., Matteucci, F., et al. 2023, *MNRAS*, **523**, 2974  
 Nelson, E. J., van Dokkum, P. G., Förster Schreiber, N. M., et al. 2016, *ApJ*, **828**, 27  
 Ness, M., & Lang, D. 2016, *AJ*, **152**, 14  
 Ness, M., Freeman, K., Athanassoula, E., et al. 2013, *MNRAS*, **430**, 836  
 Nidever, D. L., Holtzman, J. A., Allende Prieto, C., et al. 2015, *AJ*, **150**, 173  
 Nishimura, N., Sawai, H., Takiwaki, T., Yamada, S., & Thielemann, F. K. 2017, *ApJ*, **836**, L21  
 O’Neill, J. K., & Dubinski, J. 2003, *MNRAS*, **346**, 251  
 Ortalani, S., Renzini, A., Gilmozzi, R., et al. 1995, *Nature*, **377**, 701  
 Palla, M., Matteucci, F., Spitoni, E., Vincenzo, F., & Grisoni, V. 2020, *MNRAS*, **498**, 1710  
 Portail, M., Wegg, C., Gerhard, O., & Ness, M. 2017, *MNRAS*, **470**, 1233

- Queiroz, A. B. A., Anders, F., Chiappini, C., et al. 2020, [A&A](#), **638**, A76  
 Queiroz, A. B. A., Chiappini, C., Perez-Villegas, A., et al. 2021, [A&A](#), **656**, A156  
 Raha, N., Sellwood, J. A., James, R. A., & Kahn, F. D. 1991, [Nature](#), **352**, 411  
 Rich, R. M. 1988, [AJ](#), **95**, 828  
 Rich, R. M. 1990, [ApJ](#), **362**, 604  
 Rich, R. M., Howard, C., Reitzel, D. B., Zhao, H., & de Propris, R. 2008, in [Formation and Evolution of Galaxy Bulges](#), eds. M. Bureau, E. Athanassoula, & B. Barbuy, 245, 333  
 Rizzuti, F., Cescutti, G., Matteucci, F., et al. 2019, [MNRAS](#), **489**, 5244  
 Rizzuti, F., Cescutti, G., Matteucci, F., et al. 2021, [MNRAS](#), **502**, 2495  
 Rojas-Arriagada, A., Recio-Blanco, A., de Laverny, P., et al. 2017, [A&A](#), **601**, A140  
 Rojas-Arriagada, A., Zoccali, M., Schultheis, M., et al. 2019, [A&A](#), **626**, A16  
 Rojas-Arriagada, A., Zasowski, G., Schultheis, M., et al. 2020, [MNRAS](#), **499**, 1037  
 Romano, D., Chiappini, C., Matteucci, F., & Tosi, M. 2005, [A&A](#), **430**, 491  
 Romano, D., Karakas, A. I., Tosi, M., & Matteucci, F. 2010, [A&A](#), **522**, A32  
 Romano, D., Matteucci, F., Zhang, Z.-Y., Ivison, R. J., & Ventura, P. 2019, [MNRAS](#), **490**, 2838  
 Romano, D., Ferraro, F. R., Origlia, L., et al. 2023, [ApJ](#), **951**, 85  
 Salpeter, E. E. 1955, [ApJ](#), **121**, 161  
 Scalo, J. M. 1986, [Fund. Cosmic Phys.](#), **11**, 1  
 Schmidt, M. 1959, [ApJ](#), **129**, 243  
 Shen, J., Rich, R. M., Kormendy, J., et al. 2010, [ApJ](#), **720**, L72  
 Shen, L., Papovich, C., Matharu, J., et al. 2024, [ApJ](#), **963**, L49  
 Sheth, K., Elmegreen, D. M., Elmegreen, B. G., et al. 2008, [ApJ](#), **675**, 1141  
 Simonetti, P., Matteucci, F., Greggio, L., & Cescutti, G. 2019, [MNRAS](#), **486**, 2896  
 Soto, M., Rich, R. M., & Kuijken, K. 2007, [ApJ](#), **665**, L31  
 Spitoni, E., Romano, D., Matteucci, F., & Ciotti, L. 2015, [ApJ](#), **802**, 129  
 Spitoni, E., Silva Aguirre, V., Matteucci, F., Calura, F., & Grisoni, V. 2019, [A&A](#), **623**, A60  
 Spitoni, E., Verma, K., Silva Aguirre, V., et al. 2021, [A&A](#), **647**, A73  
 Tacchella, S., Carollo, C. M., Renzini, A., et al. 2015, [Science](#), **348**, 314  
 Tadaki, K.-I., Genzel, R., Kodama, T., et al. 2017, [ApJ](#), **834**, 135  
 Tsujimoto, T., & Bekki, K. 2012, [ApJ](#), **747**, 125  
 Uttenthaler, S., Schultheis, M., Nataf, D. M., et al. 2012, [A&A](#), **546**, A57  
 van de Voort, F., Schaye, J., Booth, C. M., & Dalla Vecchia, C. 2011, [MNRAS](#), **415**, 2782  
 Watson, D., Hansen, C. J., Selsing, J., et al. 2019, [Nature](#), **574**, 497  
 Wegg, C., & Gerhard, O. 2013, [MNRAS](#), **435**, 1874  
 Wegg, C., Gerhard, O., & Portail, M. 2015, [MNRAS](#), **450**, 4050  
 Weiland, J. L., Arendt, R. G., Berriman, G. B., et al. 1994, [ApJ](#), **425**, L81  
 Woods, R. M., Wadsley, J., Couchman, H. M. P., Stinson, G., & Shen, S. 2014, [MNRAS](#), **442**, 732  
 Zhao, H., Rich, R. M., & Spergel, D. N. 1996, [MNRAS](#), **282**, 175  
 Zoccali, M., Hill, V., Lecureur, A., et al. 2008, [A&A](#), **486**, 177  
 Zoccali, M., Gonzalez, O. A., Vasquez, S., et al. 2014, [A&A](#), **562**, A66  
 Zoccali, M., Vasquez, S., Gonzalez, O. A., et al. 2017, [A&A](#), **599**, A12